

# Curvature-Controlled Wrinkle Morphologies - Supporting Information

Derek Breid, and Alfred J. Crosby

Received (in XXX, XXX) Xth XXXXXXXXX 20XX, Accepted Xth XXXXXXXXX 20XX  
DOI: 10.1039/b000000x

This supplement contains calculations, figures, and discussion in support of those presented in the main text. First, we present calculations of circularity for a perfect dimple structure on a curved surface, followed by the measurements of curvature in swelling thin beams which form the basis for our overstress data, and discussion of possible sources of uncertainty in  $\sigma_c^R$ . Finally, we present images demonstrating the invariance of wrinkle patterns for spherical caps of constant radius with varying  $h$ , and data supporting the uniformity of UVO oxidation on curved surfaces.

As reported in the main text, measured circularities for even the most perfectly arranged dimple arrays on curved surfaces attained a maximum of only around 0.8. Although this may be partly ascribed to imperfectly circular dimples, the primary reason is the curvature of the spherical cap itself. Since the dimples are naturally orthogonal to the surface of the cap, dimples which form towards the side of the cap will present an elliptical projected area to the observer (Fig S1a). The average  $\Gamma$  of a model dimpled hemisphere can be estimated for various values of  $\lambda/R$ ; below, we show that 0.8 is an approximate upper bound.

We start by constructing a hexagonal grid consisting of concentric rings of hexagons, with the center containing a single hexagon and the  $n$ th ring from the center containing  $6n$  hexagons. (In reality, hexagons alone cannot tessellate a sphere, but for a small number of rings, the approximation is sufficient).

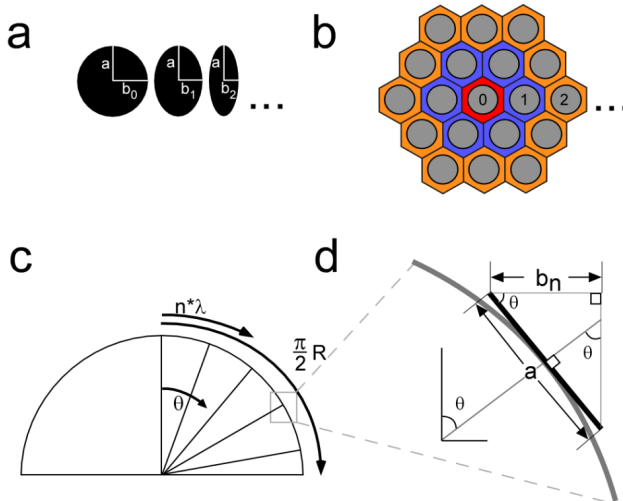


Figure S1 a) Projected elliptical areas of circles on a spherical surface. b) Perfect hexagonal array of circles. All circles in each ring ( $0, 1, 2, \dots$ ) are considered to have the same projected shape. c) Schematic of the positions of the circle centers on the surface of the hemisphere as a function of ring number  $n$ , and ring width  $\lambda$ . d) Schematic of a circle tangent to the hemisphere highlighting the relationship between the aspect ratio  $\kappa = a/b_n$  of the ellipse and the angle from the central axis of the hemisphere, which is in turn a function of  $R$ ,  $n$  and  $\lambda$ .

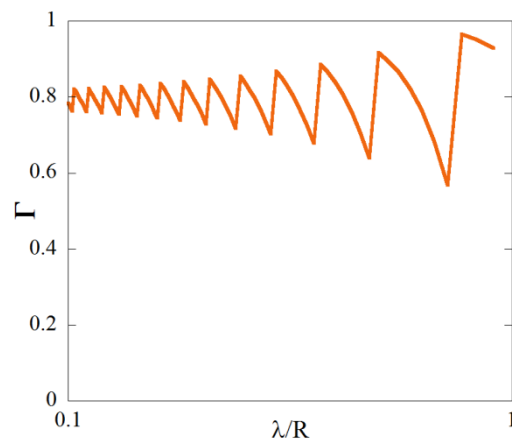
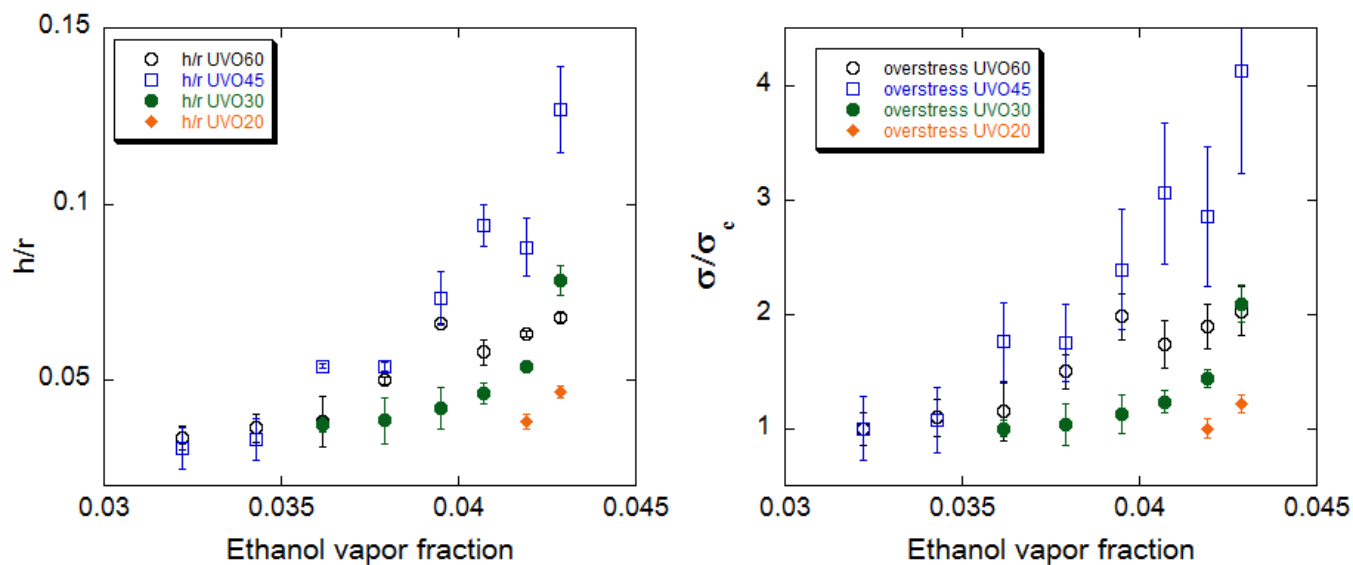


Figure S2 Plot of the calculated circularity of an array of perfect circles on a hemispherical surface as a function of  $\lambda/R$ .

We then apply these rings to the surface of a sphere, with the center hexagon located at the apex and subsequent hexagons centered at a distance of  $n\lambda$  from the apex, as shown in Fig S1c. Circles are now inscribed inside each hexagon. For simplicity, let the circles lie tangent to the hemisphere, remaining flat and not following the substrate curvature. Viewed vertically, only the minor axis ( $b_n$ ) of the projected ellipses will change, thus the ratio of the minor to major axes of the projected ellipses is  $\cos \theta$ , where  $\theta$  is the angle between the axis of symmetry of the hemisphere and the line from the center of the sphere to the center of the inscribed circle (see Fig S1d). In terms of  $\lambda$  and  $R$ , this angle is given by  $\theta = n * (\lambda/R)$ , based on fractional arc length. Since circularity is a shape-based and not a size-based quantity, we set the long axis equal to 1 and substitute the ellipse aspect ratio  $\kappa = \cos(n * (\lambda/R))$  into the approximation for the perimeter of an ellipse given by Ramanujan:<sup>1</sup>

$$P \approx \pi(1 + \kappa) \left[ 1 + \frac{3(\frac{1-\kappa}{1+\kappa})^2}{10 + \sqrt{4 - 3(\frac{1-\kappa}{1+\kappa})^2}} \right] \quad (S1)$$

Using the area of our ellipses ( $A = \pi\kappa$ ) in conjunction with Eq. 8 in the main text, we can therefore calculate an average  $\Gamma$  for any value of  $\lambda/R$ . This is plotted in Fig S2. The periodicity of the plot stems from the fact that  $n$  is an integer, and only the rings which could fit on the hemisphere were considered. A conservative threshold  $\Gamma$  of 0.3 (corresponding to  $\kappa \approx 8.5$ ) was also applied, with less circular ellipses not counted towards the overall circularity -- experimentally, ellipses near the edge of the projected area of the spherical cap are excluded from our image analysis due to loss of focus and contrast. The result is a periodic graph which centers around, and appears to eventually converge to a value of 0.8.



**Figure S3** a) Measured curling of films of PDMS corresponding to various UV time/ethanol concentration combinations. b) Normalization of the data in (a), representing the applied overstress relative to the critical buckling stress of a flat surface.

Figure S3a shows the measured curling of thin beams of UV-treated PDMS for multiple UV times in terms of  $h/r$ , where  $h$  is the beam thickness and  $r$  is the difference in radius of curvature before and after swelling. In previous work<sup>2</sup>, we demonstrated that with the assumption of linear elasticity, the overstress can be framed in terms of  $r$  alone:  $\sigma/\sigma_c = r_c/r$ . Using the lowest ethanol concentration for which buckling was observed as the critical point, values of overstress measured via film curling are given in Figure S3b. The relationship between the volume % of ethanol in the reservoir and the resulting vapor fraction is displayed in Table S1. It is interesting to note that although overstress at a given ethanol concentration generally increases with UV time, between 45 and 60 minutes, the overstress actually decreases, though  $r_c$  remains consistent with the other UV times, suggesting that  $E_f/E_s$  is not changing. One possible explanation is that the molecular network structure of the oxide film may be changing, allowing less swelling. Because we measure overstress for each  $R$  and UV time separately, this behavior does not impact our findings or conclusions in any significant way.

In addition to the radius of a spherical cap, the stress state on its surface may also depend on the height and cross-sectional area of the cap. Figure S4 depicts wrinkle patterns formed on a surfaces where  $R = 300 \mu\text{m}$  and the height of the spherical cap is varied. Even as the cap becomes very shallow, dimples remain the dominant morphology on the curved section of the wrinkling surface, while the flat section exhibits ridges. This suggests that the curvature plays a much larger role in dictating wrinkle morphology than cap aspect ratio.

Finally, in the main text, we make the assumption that UV oxidation of curved surfaces results in the formation of a uniform oxide shell. However, UV conversion of PDMS can depend greatly on the distance between the UV source and the sample and the angle of orientation between them. Based on the observation that wrinkle wavelengths are consistent between curved surfaces and the flat regions from which they protrude, we do not believe that the difference in distance to the UV source has

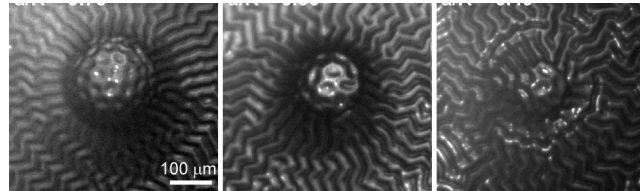


**Figure S4:** Wrinkle patterns on spherical caps of constant radius and varying height. The dimple morphology persists even as the shell becomes very shallow. However, ridges are observed to form on the flat surface. The corresponding  $h/R$  values are 0.35, 0.19, and 0.13 from left to right.

a significant impact on oxide conversion in our experiments. In addition, we have measured the effect of varying the angle of orientation of a flat PDMS surface on the resulting wrinkle wavelength (Figure S5). We found that the wavelength decreased only slightly with a 60° orientation as compared to a 0° (orthogonal) orientation. Because nearly the entire curved surface which is viewable in the top-down images which we utilize will have an orientation less than 60°, therefore we do not believe that the curved shape has a significant effect on oxide conversion.

% Ethanol in reservoir	Vapor fraction
100	0.0429
90	0.0419
80	0.0407
70	0.0395
60	0.0379
50	0.0362
40	0.0343
30	0.0322

**Table S1** Vapor fractions of ethanol corresponding to volumetric fraction of ethanol in ethanol/glycerol reservoir. Vapor fractions calculated from interpolation of experimental data by Bachmann<sup>3</sup>.

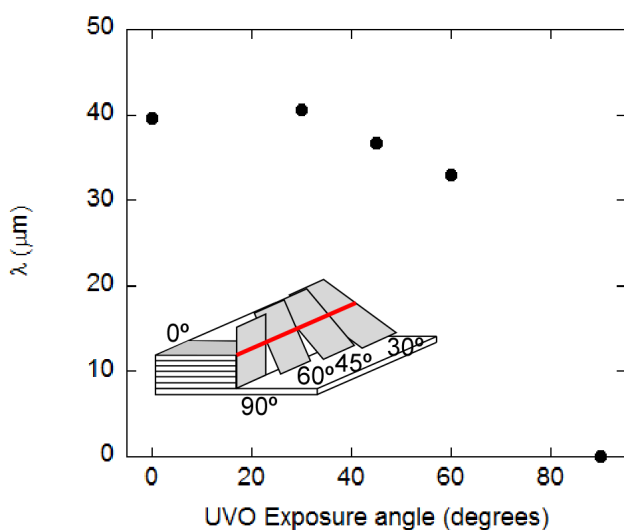


**Figure S5:** Variation of wrinkle wavelength with the angle of orientation of flat PDMS samples.

## Acknowledgement

The authors thank Vukasin Denic for assisting with measurements for Figure S5.

## Notes and references

1. Ramanujan, S. Modular Equations and Approximations to pi. *Quart. J. Math.* **45**, 350–372 (1914).
2. Breid, D. & Crosby, A. J. Effect of Stress State on Wrinkle Morphology. *Soft Matter* **7**, 4490 (2011).
- 10 3. Bachmann, W. Concerning the vapour pressure theorem of substances with a gel structure. *Z. Anorg. Allg. Chem.* 1–76 (1917).